RSC Advances

PAPER

View Article Online
View Journal | View Issue

Cite this: *RSC Adv.*, 2017, **7**, 22156

A peculiar layered 12-fold cationic coordination compound $LiInTi_2O_6$: phase relations, crystal structure and color-tunable photoluminescence†

Liu-Mei Su,[ab] Xing Fan,[ab] Ge-Mei Cai *[ab] and Zhan-Peng Jin*[ab]

Developing new hosts is one of the significant and intriguing aspects in the field of luminescence materials. Herein, we report a novel $LiInTi_2O_6$ host for phosphors in solid state lighting. The sub-solidus phase relationships, thermal stability, crystal structure, as well as composition- and temperature-dependent luminescence were investigated and discussed by means of various analytical techniques, including powder X-ray diffraction (XRD), differential scanning calorimetry (DSC), structure solution, photoluminescence excitation (PLE) and emission (PL) spectra, decay lifetime, high-temperature luminescence and chromaticity coordinates. $LiInTi_2O_6$ crystallizes in a trigonal unit cell with lattice parameters of $a = b = 5.1050(1)$ Å, $c = 28.5622(4)$ Å, and $Z = 6$ in space group $R\bar{3}m$ (No. 166), consisting of an unusual 12-fold coordination hexagonal prism structural framework. Taking $LiInTi_2O_6$ as the host, a series of Dy^{3+}/Tm^{3+} singly-doped and co-doped phosphors was successfully synthesized. With increasing Dy^{3+} concentration, the emission colors of $LiInTi_2O_6$:Tm^{3+},Dy^{3+} phosphors can be appropriately tuned from blue to yellow, going through the white region, based on the principle of energy transfer. Energy transfer efficiencies were calculated and the mechanism was confirmed to follow a resonant-type electric dipole–dipole interaction. A configuration coordinate diagram was employed to explain the thermal quenching behaviour of the white lighting phosphor. Structural characteristics and evolution trends of representative titanates were summarized, providing available information for photo/electrical materials designing.

Received 15th February 2017
Accepted 6th April 2017

DOI: 10.1039/c7ra01891f

rsc.li/rsc-advances

1. Introduction

In recent years, in recognition of the importance of saving energy, the light-emitting diode (LED) solid-state lighting industry has gradually gained much attention and has motivated many governments around the world to put scientific R&D plans in place in consideration of either energy issues or economic growth.[1–5] In particular, white LEDs, which exhibit remarkable properties that are superior to their conventional incandescent and fluorescent counterparts due to their merits of excellent reliability, high luminous efficiency, long lifetime, and low energy consumption, are accepted as the next-generation of solid-state lighting sources in the field of energy-saving technologies.[6–8] As a key component in phosphor-converted WLEDs, inorganic luminescent materials undeniably play an important role in determining the performance of solid-state lighting devices;[9] it is therefore required that they possess high conversion efficiency, appropriate emission colors as well as good stabilities. Given the high desirability for developing high-performance phosphors, abundant research efforts have been triggered to seek after novel phosphors through various strategies.[10–12] Exploring a suitable host to accommodate diverse activators to generate different colored phosphors is essential, and has stimulated researchers to devote themselves to investigating a variety of material systems, including but not limited to silicates, borates, niobates, phosphates, oxynitrides, and fluorides, leading to the discovery of a large quantity of phosphors with distinct crystal structures and fascinating photoluminescence properties.[13–17] As one of the research hotspots, exploring new compounds with special structures for phosphors is a long-standing development direction in the field of inorganic luminescent materials.

Among the variety of inorganic structural compounds, perovskites score over others due to their structural versatility and physical properties. In either the non-doped form or as a doped system, they have been applied as thermoelectric materials, catalysts, dielectrics, ferroelectrics, solid-state electrolytes, and have recently sprung up in the luminescence field.[18] A family of isomorphous layered perovskites, $(ALn)_{0.5}TiO_3$, where A represents an alkali-metal ion and Ln denotes a lanthanide, have been exploited as excellent candidates for

[a]School of Materials Science and Engineering, Central South University, Changsha, 410083, Hunan, P. R. China. E-mail: caigemei@csu.edu.cn; jin@csu.edu.cn
[b]Education Ministry Key Laboratory of Non-ferrous Materials Science and Engineering, Central South University, Changsha, 410083, Hunan, P. R. China

† Electronic supplementary information (ESI) available. See DOI: 10.1039/c7ra01891f

phosphor hosts.[19] They are proven to be have two-dimensional layered structures built by corner-shared TiO_6 octahedra, with A and Ln ions located at the interstices of TiO_6 groups. The band gap absorbing TiO_6 octahedral groups give rise to their interesting photoluminescence properties.[20] To our knowledge, on account of its similarity to lanthanide ions, in terms of ionic radius and physicochemical properties, the indium ion is found to be able to substitute for lanthanide ion in some types of compounds to form isomorphous or heteromorphic crystal structures, some of which even have outstanding luminescence properties.[21,22] Therefore, the focus of this project was the search for potential layered compounds in the Li_2O–In_2O_3–TiO_2 ternary system.

From this point of view, in this contribution, we have systematically investigated the phase relationship of the Li_2O–In_2O_3–TiO_2 ternary system *via* solid-state reactions, leading to the discovery of a new ternary compound, $LiInTi_2O_6$. To determine the crystal structure of this compound, crystallographic analysis based on powder X-ray diffraction data was implemented. Considering the underlying optical functions of a novel layered phase, especially one in which the ligand properties and ionic radius of In^{3+} is similar to rare-earth ions, blue-emitting of Tm^{3+} and yellow-emitting of Dy^{3+} ions were chosen as the co-doped activators to prepare white-light emitting $LiInTi_2O_6$ phosphors, in view of effective energy transfer existing between them in some special crystal field environments. In this work, the structure-, composition- and temperature-dependent luminescence properties of Tm^{3+} and Dy^{3+} co-doped $LiInTi_2O_6$ phosphors are investigated by means of structural analysis, photoluminescence excitation (PLE) and emission (PL) spectra, decay lifetimes, high-temperature luminescence, and chromaticity coordinates. Integrating these results indicate that $LiInTi_2O_6$ is a promising candidate as a phosphor host in solid-state lighting.

2. Experimental procedures

All polycrystalline samples with different nominal compositions in the Li_2O–In_2O_3–TiO_2 system were synthesized by conventional solid-state reaction using stoichiometric amounts of analytical reagent Li_2CO_3 (99.99%, Sinopharm Chemical Reagent Co. Ltd., Shanghai, China), In_2O_3 (99.99%, Sinopharm Chemical Reagent Co. Ltd., Shanghai, China) and TiO_2 (99.9%, Sinopharm Chemical Reagent Co. Ltd., Shanghai, China) as starting materials. Oxide powders were weighed according to different compositions in 2 ± 0.0005 g batches and mixed with an agate mortar. The mixtures were calcined in alumina crucibles at 800 °C for 12 h at a heating rate of 5 °C min^{-1}, followed by cooling inside the furnace to room temperature. Calcined powders were reground and sintered at 1000 °C for 24 h at 5 °C min^{-1}, then furnace cooled and ground for X-ray diffraction (XRD) investigation. The sintering procedure was repeated until no significant changes were observed in the XRD patterns. Rare-earth doped $LiInTi_2O_6$ phosphors were prepared *via* a solid-state reaction method as well, by adding rare-earth oxides Tm_2O_3 and Dy_2O_3 with purity of 99.99% (Alfa Aesar) into the starting material batches, according to stoichiometric ratios. Synthesis conditions were the same as that of the polycrystalline samples described above.

Phase identification of products was conducted using powder XRD patterns collected on an X-ray diffractometer (Rigaku D/MAX-2500, Rigaku Co., Tokyo, Japan) with Cu Kα radiation and a graphite monochromator operating at 40 kV and 250 mA. Powder diffraction data used for crystal structure analysis of $LiInTi_2O_6$ were gathered on a powder X-ray diffractometer (PANalytical X'Pert Pro, PANalytical B.V., Almelo, Netherlands) with Cu Kα radiation in a step scanning mode over a 2θ range from 8° to 130°, with an interval of $2\theta = 0.026°$. Structure solution for $LiInTi_2O_6$ was performed by using the JANA2006 software package.[23,24] The structure solution led to a reasonable rough structure model including all of the atomic sites, which was refined by the Rietveld method[25] using the Fullprof_suite program[26] on the basis of powder diffraction data. The thermal stability of $LiInTi_2O_6$ was investigated by the thermal analysis method using a differential scanning calorimeter (DSC) (SETSYS evolution, SETARAM INSTRUMENTATION, Caluire, France) in the temperature range of 25–1300 °C with a heating rate of 10 °C min^{-1} under an argon atmosphere.

Photoluminescence excitation (PLE) and photoluminescence emission (PL) spectra were recorded on a fluorescence spectrophotometer (Hitachi, F-7000) equipped with a 150 W xenon lamp as the excitation source. The temperature-dependent luminescence properties were measured on the same fluorescence spectrophotometer equipped with a computer-controlled heating attachment (Tianjin Orient KOJI Co. Ltd, TAP-02). Photoluminescence decay curves were obtained from a fluorescence spectrometer (Edinburgh, FLS-920) with a nF900 flash lamp as the excitation source. The CIE coordinates were calculated by using the PL data according to the CIE 1931 standard colorimetric systems. All the measurements were performed at room temperature.

3. Results and discussion

3.1. Phase relations in Li_2O–In_2O_3–TiO_2 ternary system

For the purpose of investigating phase relations in the Li_2O–In_2O_3–TiO_2 ternary system, many polycrystalline samples with certain compositions were synthesized. Phase assemblages of these products were analyzed by using powder XRD data collected at room temperature. Based on analysis of all the prepared samples, by means of retrieving phases according to ICCD-PDF (PDF-4+ 2012) and ICSD (version 2014) databases, the phases contained in mixtures were identified. Surprisingly, a new ternary compound with a set of unknown diffraction patterns detected in some TiO_2-riched samples was discovered in this work and no isostructural phases in databases were matched with it. Its formula was determined as $LiInTi_2O_6$, based on nominal composition and contact rules for phase regions. Consequently, phase regions, *i.e.* sub-solidus phase relations in the Li_2O–In_2O_3–TiO_2 ternary system were determined under the present experimental conditions, according to the results of phase identification. The phase diagram for Li_2O–In_2O_3–TiO_2 is shown in Fig. 1. It is divided into seven determinate three-phase regions by two-phase join-lines. As for the

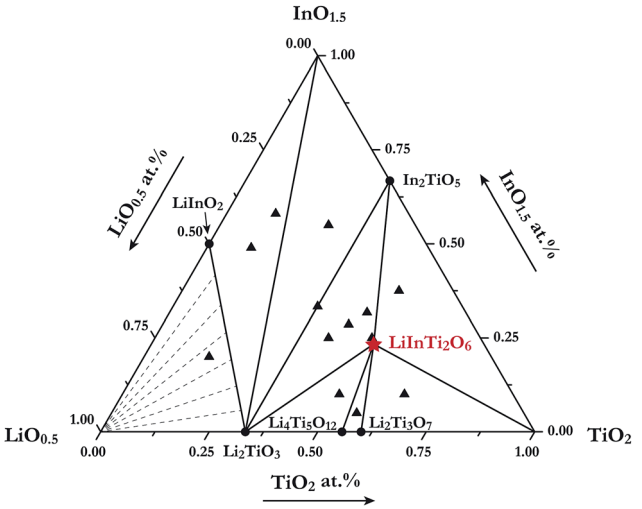

Fig. 1 Sub-solidus phase relationships of the Li_2O–In_2O_3–TiO_2 ternary system at 1000 °C. The filled triangles stand for samples located at three-phase regions and the star denotes pure $LiInTi_2O_6$.

Li_2O-rich region, marked with dashed lines in Fig. 1, it could not be determined due to Li_2O volatilizing and reacting with the corundum crucibles at high temperature.

In the In_2O_3–TiO_2 subsystem, only one binary compound, In_2TiO_5 (PDF#82-0326) was ever reported, and is now confirmed in this work. It was found to be isostructural to In_2VO_5 with an orthorhombic unit cell (S.G. *Pnma*) of $a = 7.2418$ Å, $b = 3.5018$ Å, and $c = 14.890$ Å, and its crystal structure has been refined by the Rietveld method.[27] As for the Li_2O–In_2O_3 subsystem, two binary compounds, $LiInO_2$ and Li_3InO_3, were reported.[28,29] Li_3InO_3, containing the constituent of Li_2O as high as 75 mol%, was not detected under the present experimental conditions. The Li_2O–TiO_2 binary phase diagram has been assessed by Izquierdo *et al.*[30] Four stable lithium titanates, Li_4TiO_4, Li_2TiO_3, $Li_4Ti_5O_{12}$, and $Li_2Ti_3O_7$, form in this binary system. Except for the Li_4TiO_4 phase, all the others were confirmed in this work. Li_2TiO_3 undergoes an order-disordered phase transformation from monoclinic β-phase to cubic γ-phase at about 1155 °C.[31] Herein, only the low-temperature monoclinic β-Li_2TiO_3 (PDF#33-0831) was observed. Referring to the spinel phase $Li_4Ti_5O_{12}$ (PDF#49-0207) and the ramsdellite-like phase $Li_2Ti_3O_7$ (PDF#34-0393), they decompose in the form of the peritectoid reaction above 1018 °C and eutectoid reaction below 940 °C, respectively.[30,32] As a consequence, both of these phases were detected within the range of our experimental temperature. Extrapolated to the Li_2O–In_2O_3–TiO_2 ternary system, as aforementioned, only the formation of a new ternary compound $LiInTi_2O_6$ was confirmed, and its thermal stability as well as the crystal structure is elaborated in the following section.

3.2. Thermal stability and crystal structure of $LiInTi_2O_6$

Investigation of the phase thermal stability has a great significance for materials synthesis design; therefore, we aimed to clarify the thermal stability of the newly discovered ternary compound, $LiInTi_2O_6$. The thermal analysis curve collected by DSC is shown in Fig. 2a. An obvious endothermic peak centered at 1153.5 °C was detected. Accordingly, it can be speculated that $LiInTi_2O_6$ would endothermically decompose upon heating to about 1153.5 °C. In order to verify this conjecture, some heat treatment experiments for $LiInTi_2O_6$ were performed. XRD patterns for pure phase $LiInTi_2O_6$ and its products heated at different temperature are shown in Fig. 2b. It is obvious that when heated at 1050 °C for 24 h, its XRD pattern remains unchanged. This means that $LiInTi_2O_6$ does not decompose at the present temperature. Upon being heated at 1100 °C for 24 h, some tiny diffraction peaks assigned to In_2TiO_5 (PDF#82-0326) and TiO_2 (PDF#77-0440) turned up, in addition to the content of $LiInTi_2O_6$ decreasing, thus indicating that $LiInTi_2O_6$ decomposition was initiated. When heated at higher the temperature of 1200 °C, this compound completely decomposed into In_2TiO_5, TiO_2 and $Li_2Ti_3O_7$ (PDF#34-0393). Consequently, a four-phase transformation reaction of $LiInTi_2O_6 \rightarrow TiO_2 + In_2TiO_5 + Li_2Ti_3O_7$ is considered to take place in the range of 1100–1200 °C. According to the DSC curve, its temperature was determined to be about 1153.5 °C. Besides, the sharp endothermic peak with the minimum at 1292 °C corresponds to the incongruently melting point of $Li_2Ti_3O_7$.[30,32]

The XRD pattern of $LiInTi_2O_6$ can be indexed to a trigonal unit cell with lattice parameter of $a = b = 5.1050(1)$ Å, $c = 28.5622(4)$ Å, and $Z = 6$ in space group $R\bar{3}m$ (No. 166) by using the WinCSD program package.[33] The rough structural model of $LiInTi_2O_6$ solved by the charge-flipping method[34] consists of 6 crystallographic sites for distinct atoms: one lithium site, one indium site, two titanium sites, and two sites for oxygen. Based on this unprocessed crystal structure, further structural modification *via* Rietveld refinement was performed. The final refined plot for $LiInTi_2O_6$ is depicted in Fig. 3 and the refined crystallographic parameters and reliability factors are listed in Table 1. Primary reliability factors were converged to $R_B = 5.66\%$, $R_p = 2.88\%$, $R_{wp} = 4.39\%$, and $S = 2.31$, indicating that this crystal structure for $LiInTi_2O_6$ is reasonably accepted. Structural parameters including atomic occupations and bond lengths for $LiInTi_2O_6$ are listed in Table 2 and 3, respectively. Refinement shows that titanium ions occupy two 6c sites; the other 6c site is co-occupied by lithium and titanium ions, and the remaining 6c site is a mixed In/Li/Ti site. It is worth mentioning that according to the atomic occupancies of refinement, the actual formula of this new ternary compound should be $Li_{0.856}In_{0.92}Ti_{1.672}O_6$, which deviated from stoichiometry; we approximately adopted $LiInTi_2O_6$ to denote this new ternary compound in this context.

The crystal structure and coordination environments for cation sites of $LiInTi_2O_6$ are presented in Fig. 4. All the cations appear to have the same coordination environments, *i.e.* they are all coordinated with 12 oxygens to form distorted 12-fold coordination hexagonal prisms depending on the central cations. In three-dimensional structural framework, mixed hexagonal prisms stack layer by layer along the *c* axis in the form of edge-sharing and face-sharing. Titanium ions respectively occupying two distinct 6c sites, denoted as Ti3 and Ti4 in Fig. 4, alternately pile up along the *c* axis and are separated by (Li/Ti)O_{12} and (In/Li/Ti)O_{12} hexagonal prisms. In every TiO_{12}

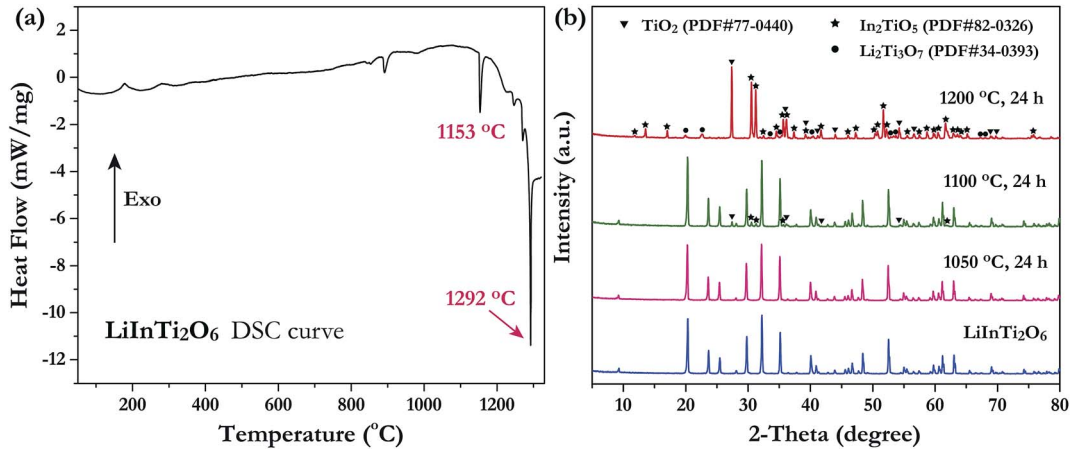

Fig. 2 (a) The DSC curve of $LiInTi_2O_6$. (b) XRD patterns of $LiInTi_2O_6$ heated at 1050, 1100 and 1200 °C, respectively, compared to the pure phase pattern.

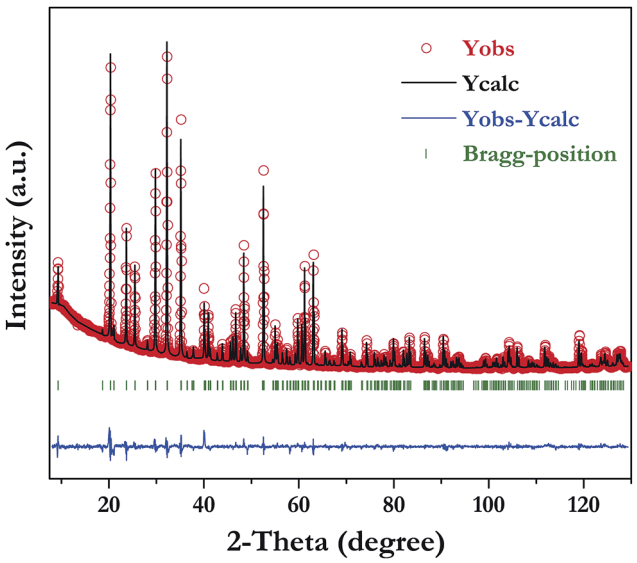

Fig. 3 Rietveld refinement of XRD data for $LiInTi_2O_6$.

polyhedral layer, hexagonal prisms share three side-faces with each other at 120° angles to form hexagonal prismatic holes. By means of face-sharing, TiO_{12} polyhedra spread out towards the *a* and *b* axis to form two-dimensional sheets.

3.3. Color-tunable luminescence properties of $LiInTi_2O_6$:Tm^{3+},Dy^{3+} phosphors

3.3.1. Photoluminescence properties of Dy^{3+} and Tm^{3+} singly-doped $LiInTi_2O_6$ phosphors. A series of Dy^{3+} and Tm^{3+} singly-doped $LiInTi_2O_6$ phosphors were synthesized *via* high-temperature solid-state reaction in our work. The phase assemblage and purity of the as-prepared phosphors were investigated by analyzing their XRD patterns and Rietveld structural refinement results. Considering the similar valences and effective ionic radii of Dy^{3+} ($r = 0.91$ Å) and Tm^{3+} ($r = 0.87$ Å) to In^{3+} ($r = 0.81$ Å), it was expected that RE ions would be

Table 1 Experimental parameters of powder X-ray diffraction, and refined crystallographic data of $LiInTi_2O_6$

Chemical Formula	$LiInTi_2O_6$
Diffractometer	X'Pert Pro, PANalytical
Radiation type	Cu Kα, $\lambda = 1.54060$ Å
2θ interval (°)	8.021–129.987
Step size of 2θ (°)	0.026
Space group	$R\bar{3}m$ (No. 166)
Z	6
a (Å)	5.1050(1)
b (Å)	5.1050(1)
c (Å)	28.5622(4)
V (Å^3)	644.64(2)
Number of points	4692
Number of reflections	350
Number of structure parameters	118
Number of profile parameters	12
R_B[a] (%)	5.66
R_p[b] (%)	2.88
R_{wp}[c] (%)	4.39
S[d]	2.31

[a] $R_B = \sum|I_{O,h} - I_{C,h}|/\sum|I_{O,h}|$. [b] $R_P = \sum|y_i - y_{C,i}|/\sum y_i$. [c] $R_{wp} = \left[\sum w_i|y_i - Y_{C,i}|^2 \Big/ \sum w_i y_i^2\right]^{\frac{1}{2}}$. [d] $S = R_{wp}/R_{exp}$.

Table 2 Wyckoff positions, atomic coordinates, and occupancies of $LiInTi_2O_6$

Atom	Site	x	y	z	B_{iso} (Å^2)	Occupancy
Li1	6c	0	0	0.4190(4)	1.1(3)	0.814(1)
Ti1	6c	0	0	0.4190(4)	1.1(3)	0.186(1)
In	6c	0	0	0.0741(1)	0.6(4)	0.916(1)
Li2	6c	0	0	0.0741(1)	0.6(4)	0.042(1)
Ti2	6c	0	0	0.0741(1)	0.6(4)	0.042(1)
Ti3	6c	0	0	0.3255(2)	0.5	0.743(1)
Ti4	6c	0	0	0.1819(1)	0.5	0.743(1)
O1	36i	−0.0320(14)	0.3157(17)	0.6998(3)	1.1(2)	0.5
O2	36i	−0.0174(17)	0.6837(15)	0.1321(3)	1.7(2)	0.5

Table 3 Bond lengths for $LiInTi_2O_6$ compound

Bond	Length (Å)	Bond	Length (Å)
Li1/Ti1–O1 (×6)	2.1857	In/Li2/Ti2–O1 (×6)	2.1698
Li1/Ti1–O2 (×6)	2.2645	In/Li2/Ti2–O2 (×6)	2.2839
Average	2.2251	Average	2.2269
Ti3–O1 (×6)	1.8444	Ti4–O2 (×6)	1.7946
Ti3–O1 (×6)	1.9736	Ti4–O2 (×6)	2.1201
Average	1.9090	Average	1.9574

preferred to occupy the In^{3+} sites in the $LiInTi_2O_6$ host. As can be seen from Fig. S1 in the ESI,† XRD patterns of the representative phosphors of $LiInTi_2O_6$:0.01Dy^{3+} and $LiInTi_2O_6$:0.02-Tm^{3+} show good consistency with the pattern of $LiInTi_2O_6$ and no impurities were detected, implying that the doped RE ions are completely dissolved into the host lattice of $LiInTi_2O_6$ and do not induce any significant changes in the crystal structure. This conclusion could also be effectively confirmed by the Rietveld refinement analysis. Refined patterns for representative samples are revealed in Fig. S2.† On account of the larger RE ions, Dy^{3+}/Tm^{3+}, replacing In^{3+} ions, expansions of unit cells were observed in phosphors, compared to the host.

Fig. 5a shows the room temperature PLE and PL spectra for the Dy^{3+}-activated $LiInTi_2O_6$ phosphor. When monitoring the characteristic emission of Dy^{3+} at 580 nm ($^4F_{9/2}$–$^6H_{13/2}$), the PLE spectrum of $LiInTi_2O_6$:0.01Dy^{3+} consists of a broad charge-transfer excitation band (CTB) and a series of sharp peaks in the range of 300–500 nm. Since Dy^{3+} in oxides does not have charge-transfer transition bands longer than 200 nm,[35,36] the CTB in PLE spectrum of $LiInTi_2O_6$:0.01Dy^{3+} is mainly attributed to the absorption of Ti–O polyhedra in the host.[37,38] The narrow excitation peaks are assigned to the f–f electronic transitions from the ground state $^6H_{15/2}$ to distinct excited states (marked in Fig. 5a) of Dy^{3+} within its $4f^9$ electron configuration.[38,39] Two excitation transitions at 353 nm ($^6H_{15/2}$–$^6P_{7/2}$) and 454 nm ($H_{15/2}$–$^4I_{15/2}$) have comparable emission intensities, indicating that $LiInTi_2O_6$:Dy^{3+} phosphors are potential light-converting candidates for UV-LED and blue-LED applications in solid-state lighting. Upon excitation at 353 nm and 454 nm, the PL spectra of $LiInTi_2O_6$:0.01Dy^{3+} exhibit characteristic emissions of Dy^{3+}. Evidently, the emission intensity of the electric dipole transition ($^4F_{9/2}$–$^6H_{13/2}$) located in the yellow region and centered at 580 nm is significantly higher than that of the blue emission peaking at 491 nm, which originated from a magnetic dipole transition of $^4F_{9/2}$–$^6H_{15/2}$. Generally, the former transition is hypersensitive to the crystal-field environment of Dy^{3+}.[39,40] When Dy^{3+} occupies a lattice site that deviates from an inversion center, the $^4F_{9/2}$–$^6H_{13/2}$ transition of yellow emission dominates and has a much higher intensity than the blue emission,[41] therefore confirming that Dy^{3+} ions in $LiInTi_2O_6$:Dy^{3+} phosphors occupy the non-centrosymmetric 6c (C_{3v}) sites, which are away from an inversion center in the centrosymmetric space group $R\bar{3}m$. Fig. 5b presents the PL spectra of $LiInTi_2O_6$:$x$$Dy^{3+}$ phosphors with different Dy^{3+} doping concentrations under the excitation of 353 nm, as well as the dependence of emission intensities on Dy^{3+} concentrations (inset). As seen, the emission spectra profiles and the intensity ratio of yellow to blue emission (Y/B = 6.1–6.5) are almost unaltered over the full Dy^{3+}-doped concentration range, indicating the surrounding environments for Dy^{3+} are not significantly changed as its concentration increased. As shown in the inset of Fig. 5b, the concentration quenching for $LiInTi_2O_6$:$x$$Dy^{3+}$ phosphors occur at $x = 0.013$, owing to cross relaxation between the energy levels of Dy^{3+}, *i.e.* energy transfer from a transition of $^4F_{9/2}$–$^6F_{3/2}$ in one Dy^{3+} to another Dy^{3+}, with the transition of $^6H_{15/2}$–$^6F_{11/2}$ of matching energy.

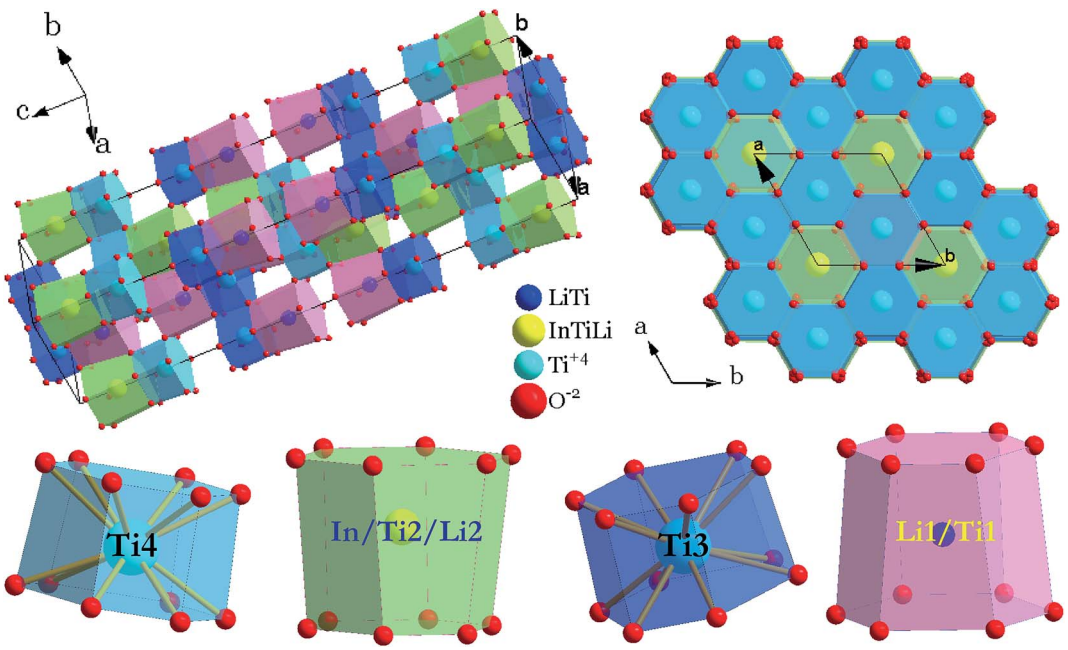

Fig. 4 Crystal structure of $LiInTi_2O_6$ and coordination polyhedra of cation sites.

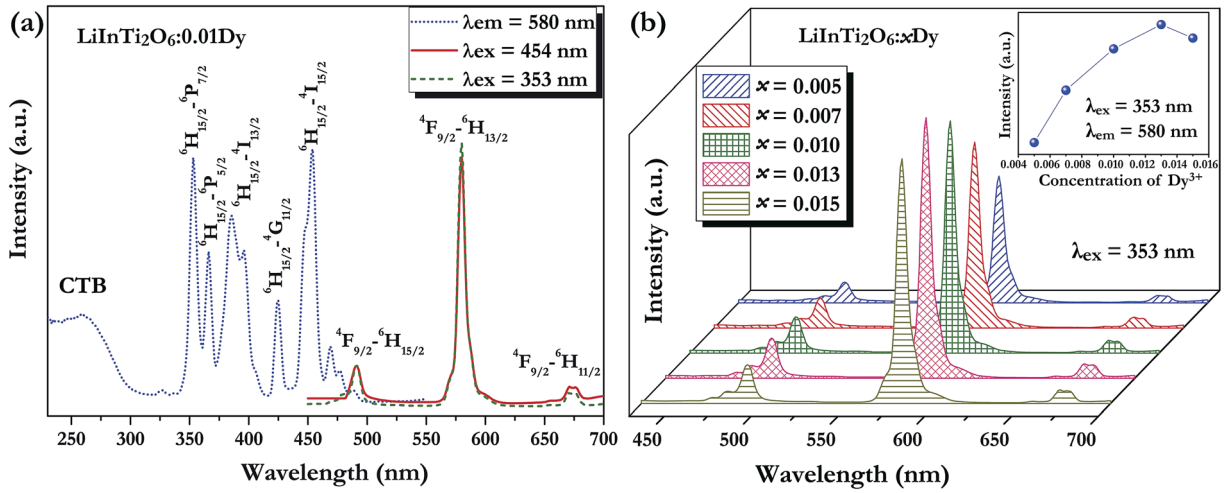

Fig. 5 (a) Photoluminescence excitation and emission spectra of $LiInTi_2O_6$:0.01Dy^{3+} and (b) PL spectra of $LiInTi_2O_6$:xDy^{3+} phosphors as a function of Dy^{3+} doping content (x) excited at 353 nm. The inset shows the dependence of emission intensities on x.

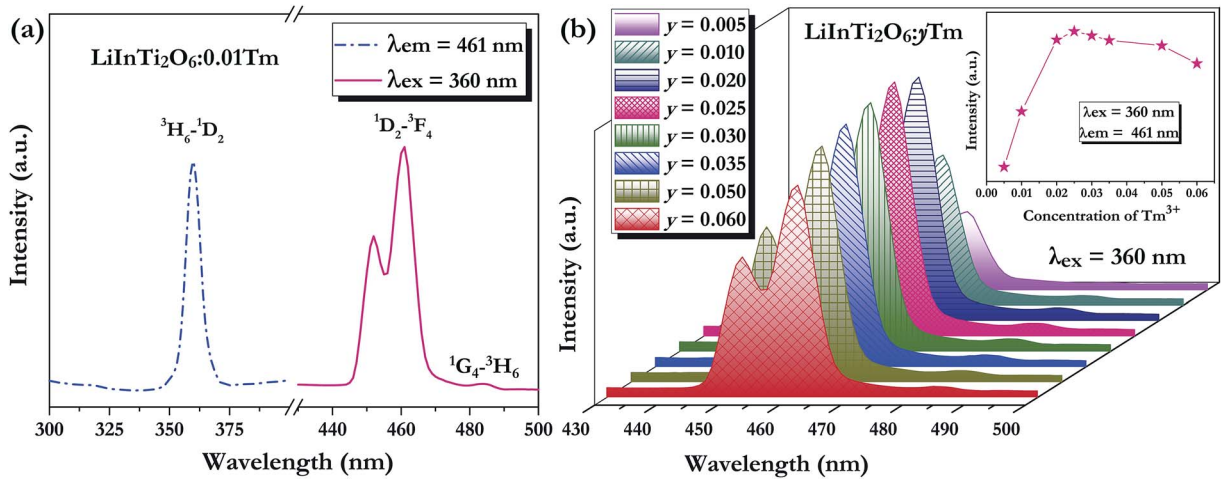

Fig. 6 (a) PLE and PL spectra of $LiInTi_2O_6$:0.01Tm^{3+} and (b) PL spectra of $LiInTi_2O_6$:yTm^{3+} phosphors as a function of Tm^{3+} doping content (y) excited at 360 nm. The inset shows the dependence of emission intensities on y.

As for the Tm^{3+}-activated $LiInTi_2O_6$ phosphors, their PLE and PL spectra are depicted in Fig. 6. The PLE spectrum of $LiInTi_2O_6$:0.01Tm^{3+} monitored at 461 nm simply exhibits a characteristic excitation peak of Tm^{3+} at 359 nm, which is generated from an f–f transition of $^3H_6$–$^1D_2$ within the $4f^{12}$ configuration of Tm^{3+}. Under the excitation of 360 nm, the PL spectrum shows an intense blue emission at 461 nm, attributed to the electronic dipole transition of $^1D_2$–$^3F_4$, as well as a weak emission at 484 nm ($^1G_4$–$^3H_6$). With increased Tm^{3+} doping concentration, emission spectra profiles for $LiInTi_2O_6$:yTm^{3+} remained invariable and emission intensities of peaks at 459 nm gradually increased with the increasing concentration, and obviously decreased after reaching the maximum at $y = 0.025$, owing to the concentration quenching effect (inset in Fig. 6b).

3.3.2. Tunable photoluminescence properties and energy transfer of Dy^{3+}/Tm^{3+} co-doped $LiInTi_2O_6$ phosphors. Generally, enhancing luminescence and tuning colors for light-conversion phosphors can be effectively carried out by means of energy transfer from sensitizers to activators. As shown in Fig. 7, the PLE spectrum of $LiInTi_2O_6$:Dy^{3+} and the PL spectrum of $LiInTi_2O_6$:Tm^{3+} present a significant overlap in the range of 445–470 nm, covering the emission band of Tm^{3+} peaking at 461 nm ($^1D_2$–$^3F_4$), and the excitation band of Dy^{3+} peaking at 454 nm ($^6H_{15/2}$–$^4I_{15/2}$). Spectral overlap indicates that effective energy transfer from Tm^{3+} to Dy^{3+} is expected in $LiInTi_2O_6$:Tm^{3+},Dy^{3+} phosphors. Accordingly, white-light emission could be realized in single-component Tm^{3+}/Dy^{3+} co-activated $LiInTi_2O_6$ phosphors under UV light excitation, by virtue of adjusting the concentrations of Tm^{3+} with blue emission and Dy^{3+} with yellow emission, based on the principle of energy transfer.

In order to achieve white-light emission in single-phase Tm^{3+}/Dy^{3+} co-activated $LiInTi_2O_6$ phosphors, appropriate doping ratios of activators and excitation wavelengths are

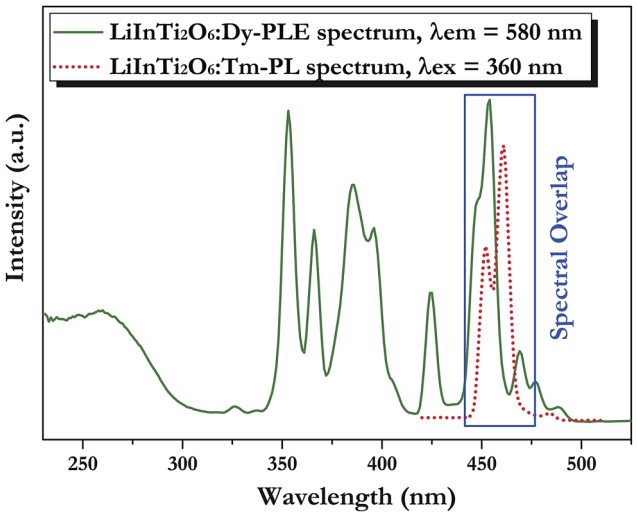

Fig. 7 Spectral overlap between PL spectrum of $LiInTi_2O_6$:Tm^{3+} (red dotted line) and PLE spectrum of $LiInTi_2O_6$:Dy^{3+} (olive solid line).

required. In this work, the more the Tm^{3+} is doped, the less the Dy^{3+} can be co-doped. Based on scores of trial and error experiments, the co-doping concentration of Tm^{3+} was determined to be 0.01 to obtain white-light emission under UV excitation, in spite of its optimal doping concentration being 0.025 in the $LiInTi_2O_6$ host. Consequently, a series of $LiInTi_2O_6$:0.01-Tm^{3+},$x$$Dy^{3+}$ (x = 0, 0.003, 0.005, 0.007, 0.01, 0.013, and 0.015) phosphors with different Dy^{3+} concentrations were synthesized and their photoluminescence properties were investigated. As seen in Fig. S1 and S2,† Tm^{3+} and Dy^{3+} can be simultaneously incorporated into the $LiInTi_2O_6$ host, without causing any changes in the crystal lattice. Fig. 8 shows the PL spectra of as-prepared samples under 360 nm excitation. Obviously, all the PL spectra for Dy^{3+}/Tm^{3+} co-doped $LiInTi_2O_6$ phosphors consist of characteristic emission bands for both Tm^{3+} and Dy^{3+}. With the concentration of Dy^{3+} increasing, the emission intensities of Tm^{3+} centered at 461 nm monotonically decrease, whereas those of Dy^{3+} gradually increase. This observed variation in trend can also be seen from the dependence of emission intensities on Dy^{3+} doping concentrations in the inset of Fig. 8. This variation supports the occurrence of effective energy transfer from Tm^{3+} to Dy^{3+} in $LiInTi_2O_6$:Tm^{3+},Dy^{3+} phosphors. This kind of energy transfer between the sensitizer of Tm^{3+} and the activator of Dy^{3+} is mainly ascribed to the energy of the emission transition $^1D_2$–$^3F_4$ for Tm^{3+} matching well with the excitation transition $^6H_{15/2}$–$^4I_{15/2}$ for Dy^{3+}. The energy transfer process between proposed energy levels of Dy^{3+} and Tm^{3+} are illustrated in Fig. 9. Upon 359 nm excitation, electrons in Tm^{3+} ions are excited from the $^3H_6$ ground state to the $^1D_2$ excited state. Some energy is then released on account of excited electrons jumping down to the $^3F_4$ excitation state to emit blue light, while residual energy is absorbed by electrons of Dy^{3+} in the ground state $^6H_{15/2}$, to jump up to the $^4I_{15/2}$ excited state, due to energy matching. Subsequently, there is non-radiative relaxation to the $^4F_{9/2}$ level and the generation of characteristic emission transitions of Dy^{3+} ions to emit colourful lights.

Generally speaking, the energy transfer process can be revealed by the photoluminescence decay behaviour of phosphors; therefore, in order to further confirm the presence of energy transfer from Tm^{3+} ions to Dy^{3+} ions in $LiInTi_2O_6$:-Tm^{3+},Dy^{3+} phosphors, photoluminescence decay curves were investigated. Fig. 10a shows the decay curves of Tm^{3+} emission in $LiInTi_2O_6$:0.01Tm^{3+},$x$$Dy^{3+}$ phosphors recorded at 461 nm under the excitation of 360 nm. It was found that all the decay curves associated with the emission transition of $^1D_2$–$^3F_4$ at 461 nm can be well fitted to a second-order exponential decay function:

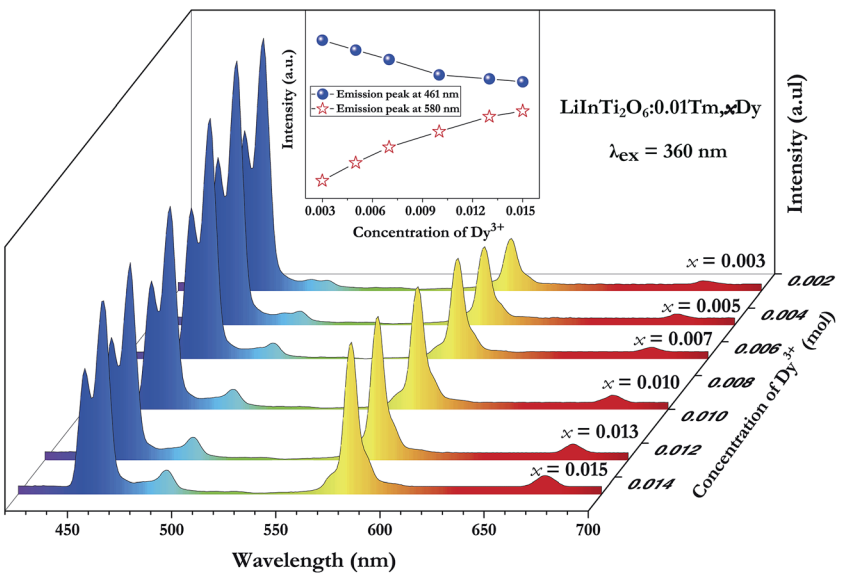

Fig. 8 PL spectra of $LiInTi_2O_6$:0.01Tm^{3+},$x$$Dy^{3+}$ phosphors excited at 360 nm with different Dy^{3+} doping concentrations. Inset shows the dependence of emission intensities of peaks at 461 nm and 580 nm on x.

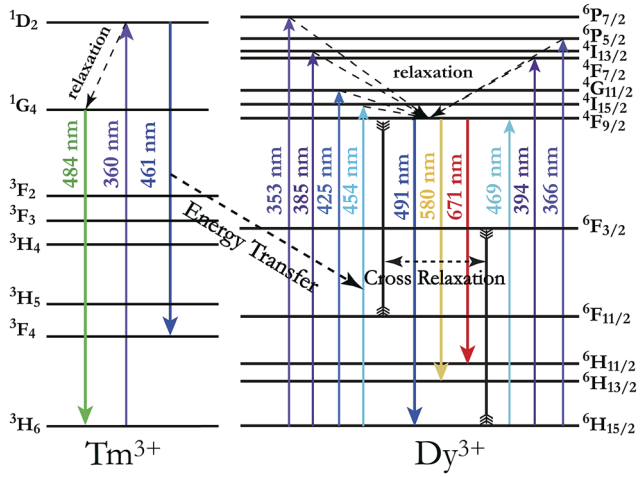

Fig. 9 Schematic energy level diagram illustrating characteristic excitation and emission of Tm^{3+} and Dy^{3+}, and energy transfer process from Tm^{3+} to Dy^{3+}.

$$I(t) = A_1 \exp\left(-\frac{t}{\tau_1}\right) + A_2 \exp\left(-\frac{t}{\tau_2}\right) + I_0 \quad (1)$$

where $I(t)$ stands for the emission intensity at time t, A_1 and A_2 are constants, and τ_1 and τ_2 denote the short and long decay lifetimes for exponential components, respectively. As a consequence, according to equation of $\tau = (A_1\tau_1^2 + A_1\tau_1^2)/(A_1\tau_1 + A_1\tau_1)$, the average lifetimes for $LiInTi_2O_6$:Tm^{3+},xDy^{3+} with $x = 0$, 0.003, 0.005, 0.007, 0.01, 0.013, and 0.015 were determined to be 23.05, 18.79, 18.20, 18.05, 16.10, 16.34, and 16.24 μs, respectively, indicating that they are short enough for potential application in solid-state lighting.[42] Apparently, decay lifetimes for Tm^{3+} monotonically decreased as the concentration of Dy^{3+} increased, which strongly demonstrates the existence of energy transfer from Tm^{3+} to Dy^{3+}. Energy transfer effectiveness can be estimated from lifetimes by calculating the energy transfer rate and energy transfer efficiency.[43,44] For Tm^{3+} singly-doped and Tm^{3+}/Dy^{3+} co-doped $LiInTi_2O_6$ phosphors, the luminescence decay process can be separately written as follows:

$$\frac{dC_{Tm}^*}{dt} = -\kappa_1 C_{Tm}^* = -\tau_0^{-1} C_{Tm}^* \quad (2)$$

$$\frac{dC_{Tm}^*}{dt} = -(\kappa_1 + \kappa_{ET}) C_{Tm}^* = -\tau_1^{-1} C_{Tm}^* \quad (3)$$

where C_{Tm}^* stands for energy state concentrations of Tm^{3+}; κ_1 and κ_{ET} are rate constants for photoluminescence of Tm^{3+} and energy transfer from Tm^{3+} to Dy^{3+}, respectively; τ_0 and τ_1 are decay lifetimes of sensitizer Tm^{3+} in the absence and presence of activator Dy^{3+}, respectively. According to eqn (2) and (3), the rate constant κ_{ET} and energy transfer efficiency η_{ET} can be calculated as follows:

$$\kappa_{ET} = \tau_1^{-1} - \kappa_1 = \tau_1^{-1} - \tau_0^{-1} \quad (4)$$

$$\eta_{ET} = \frac{\kappa_{ET} C_{Tm}^*}{\kappa_1 C_{Tm}^* + \kappa_{ET} C_{Tm}^*} = \frac{\tau_1^{-1} - \tau_0^{-1}}{\tau_1^{-1}} = 1 - \frac{\tau_1}{\tau_0} \quad (5)$$

The dependence of lifetimes and energy transfer efficiencies on Dy^{3+} concentration is plotted in Fig. 10b, from which one can see that the average lifetimes decreased and energy transfer efficiencies generally increased with the increment of Dy^{3+} content, indicating energy transfer from Tm^{3+} to Dy^{3+}.

3.3.3. Energy transfer mechanism and thermal quenching behaviour. In general, resonant-type energy transfer from a sensitizer to an activator in phosphors is realized either by virtue of the exchange interaction or the electric multipolar interaction. When critical distances between sensitizers and activators are shorter than 5 Å, the former interaction is dominant, while the latter does not generate effects. According to the concentration quenching method proposed by G. Blasse, the critical distance influencing energy transfer between the sensitizer Tm^{3+} and the activator Dy^{3+} in $LiInTi_2O_6$:0.01-Tm^{3+},xDy^{3+} phosphors can be estimated using the following formula:[45]

$$R_c \approx 2\left(\frac{3V}{4\pi x_c Z}\right)^{\frac{1}{3}} \quad (6)$$

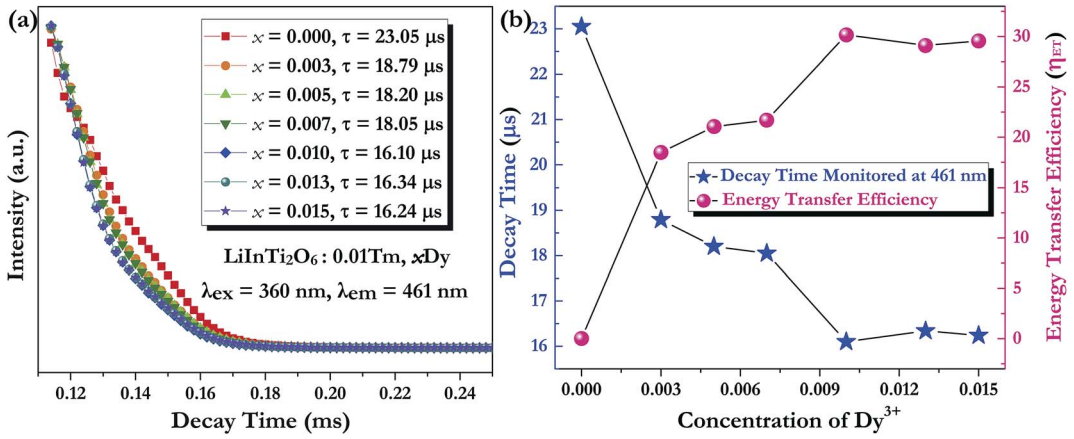

Fig. 10 (a) Photoluminescence decay curves of Tm^{3+}, monitored at 461 nm under the excitation of 360 nm, with the variation of x. (b) The dependence of lifetime and energy transfer efficiency from Tm^{3+} to Dy^{3+} on x in $LiInTi_2O_6$:0.01Tm^{3+},xDy^{3+} phosphors.

where V, x_c, and Z stand for the unit cell volume, the critical concentration, and the number of lattice sites per unit cell that can be occupied by activators, respectively. For $LiInTi_2O_6$:0.01-Tm^{3+},xDy^{3+} phosphors, the values of V and Z are respectively determined to be $V = 644.64$ Å^3 and $Z = 6$. As for x_c, it is usually defined as the sum of sensitizer and activator concentration at which the energy transfer efficiency is equal to 50%.[46] In this work, the energy transfer efficiency does not reach the point of 50%, thus, x_c is determined to be 0.025, the sum of Tm^{3+} concentration 0.01 and the maximum doped content of Dy^{3+} 0.015. Therefore, the critical distance between Tm^{3+} and Dy^{3+} in $LiInTi_2O_6$:0.01Tm^{3+},xDy^{3+} phosphors is calculated to be 20.17 Å, much longer than 5 Å, indicating that the energy transfer mechanism is governed by electric multipolar interactions. Furthermore, electric multipolar interactions are subdivided into three categories: dipole–dipole (d–d), dipole–quadrupole (d–q), and quadrupole–quadrupole (q–q) interactions. Ultimately, which one of these three kinds of interactions is dominant can be verified on the basis of Dexter's energy transfer formula and Reisfeld's approximation, according to the following relation:[47]

$$\frac{I_0}{I} \propto C^{n/3} \quad (7)$$

where I_0 and I denote PL intensities of the sensitizer Tm^{3+} in absence and presence of the activator Dy^{3+}, respectively; C is the sum of Tm^{3+} and Dy^{3+} concentrations, and n = 6, 8, and 10 correspond to d–d, d–q, and q–q interactions, respectively. The dependence of I_0/I on $C^{6/3}$, $C^{8/3}$, and $C^{10/3}$ for $LiInTi_2O_6$:0.01-Tm^{3+},xDy^{3+} phosphors is illustrated in Fig. 11. All the plots are fitted with linear functions and when $n = 6$ ($R^2 = 0.96395$), there is a better match to linear behaviour, implying that the energy transfer from Tm^{3+} to Dy^{3+} conforms to a non-radiative electric dipole–dipole (d–d) interaction mechanism. This energy transfer mechanism of Tm^{3+} to Dy^{3+} in $LiInTi_2O_6$ is similar to the case of Tm^{3+} to Dy^{3+} in $InNbO_4$.[22]

The energy transfer process is a feasible route to tuning the emission colors of light-conversion phosphors for practical applications. Consequently, a white light emission could be realized *via* energy transfer by adjusting the ratio of Tm^{3+} and Dy^{3+} to a suitable value in a single-component $LiInTi_2O_6$:-Tm^{3+},Dy^{3+} phosphor. In order to demonstrate the practical application of $LiInTi_2O_6$:Tm^{3+},Dy^{3+} phosphors, a 366 nm UV lamp was used to irradiate the phosphors. As a consequence, a series of digital lighting photographs was obtained, as shown in Fig. 12. For comparison, correlated Commission International de I'Eclairage (CIE) chromaticity coordinates with different doping concentrations, determined on the basis of their corresponding PL spectra under excitation of 366 nm, are also listed. It was found that the Tm^{3+} singly-doped $LiInTi_2O_6$ phosphor (point 1 in Fig. 12) exhibits blue-light emission with CIE chromaticity coordinate (0.1606, 0.0864), while the Dy^{3+} singly-doped $LiInTi_2O_6$ phosphor (point 8) shows yellow light with CIE chromaticity coordinate (0.4483, 0.4312). As for Tm^{3+}/Dy^{3+} co-doped $LiInTi_2O_6$ phosphors, the colour tone can be tuned from blue, with chromaticity coordinate of (0.2496, 0.2041), to white, with (0.3340, 0.3104), across the white lighting region with an increase in Dy^{3+} doping concentrations based on the principle of energy transfer from Tm^{3+} to Dy^{3+}. These results suggest that $LiInTi_2O_6$:Tm^{3+},Dy^{3+} phosphors can be effectively excited with UV light and they are potential single-component blue-yellow tunable candidates for possible applications in white-light-emitting UV-LEDs for solid-state lighting.

As is well known, lighting devices usually suffer from thermal invalidation with the increase in service time at high temperature, and some peculiar behaviour may be encountered. This phenomenon also applies to LEDs, which influences the photoluminescence of the light-conversion components,

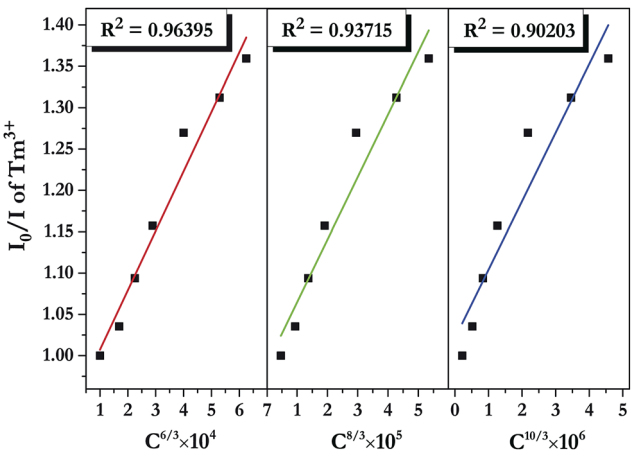

Fig. 11 Dependence of I_0/I of Tm^{3+} on the sum of Tm^{3+} and Dy^{3+} concentrations $C^{6/3}$, $C^{8/3}$, and $C^{10/3}$ in $LiInTi_2O_6$:0.01Tm^{3+},xDy^{3+} phosphors.

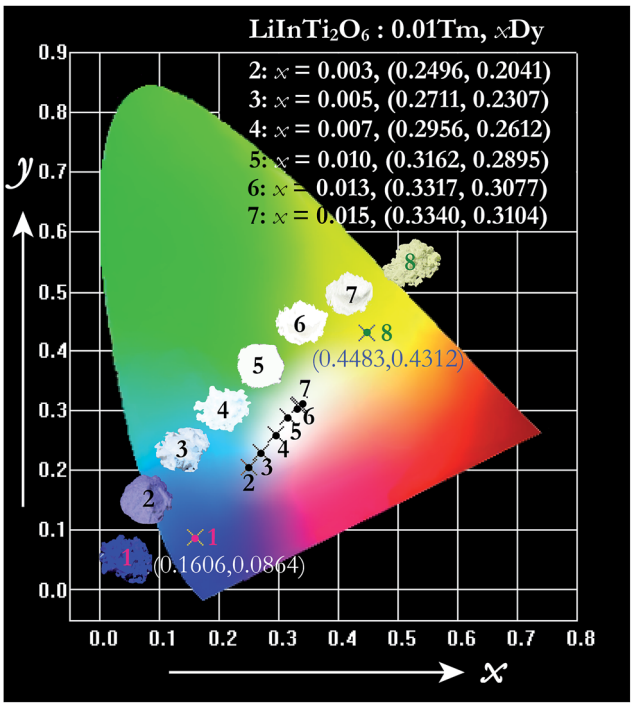

Fig. 12 CIE chromaticity diagram of $LiInTi_2O_6$:0.01Tm^{3+} (point 1), $LiInTi_2O_6$:0.015Dy^{3+} (point 8), and $LiInTi_2O_6$:0.01Tm^{3+},xDy^{3+} phosphors (point 2–7) under 366 nm UV excitation.

i.e. phosphors. Thus, temperature stability, *i.e.* thermal quenching behaviour of photoluminescence, is an important issue to be considered in evaluating the luminescence properties of phosphors. The temperature-dependent emission spectra for the as-prepared $LiInTi_2O_6$:0.01Tm^{3+},0.015Dy^{3+} phosphor under 366 nm excitation was carried out from 25 to 300 °C, and normalized emission intensities of Tm^{3+} and Dy^{3+} as a function of temperature are presented in Fig. 13a. As can be seen, the positions of the maximum peaks for Tm^{3+} originating from the $^1D_2$–$^3F_4$ transition are red-shifted and the emission intensity abnormally increases with the increase in temperature to 300 °C; whereas, the PL intensity at 580 nm for Dy^{3+} significantly decreases as temperature increases, ascribed to thermal quenching. The red-shift occurs because with the increase in temperature, the host lattice expands due to the thermal expansion effect; thus, the bond lengths between activators and ligands increase, leading to a decrease in the crystal field, which decreases the transition energy.[48,49] In general, at a high temperature, the population density of thermal active phonons increases, and the electron–phonon interaction is intense, causing an increase in the thermally activated nonradiative transition probability; as a consequence, emission intensity decreases.[48,49] However, the abnormal dependence of emission intensity on temperature for Tm^{3+}, which occurs in $LiInTi_2O_6$:Tm^{3+},Dy^{3+} phosphors results from a phenomenon known as negative thermal quenching (NTQ).[50,51] Similar NTQ phenomena are also observed in other reported luminescent materials.[49,52,53] Temperature-dependent electron numbers in eigenstates, which dominantly affect the PL intensity, are contributed by four components: electron relaxation, radiative transition, nonradiative transition and thermal excitation. When the energy separation between the initial excited state and some middle excited states is comparable to the temperature of the system, thermal excitation of electrons from the latter states to the former state is significant.[54] Meanwhile, the energy eigenvalues for these middle excited states are smaller than that of the initial state. Therefore, thermal excitation of electrons in Tm^{3+} accounts for the NTQ phenomenon. As for Dy^{3+}, as seen in Fig. 13a, the PL intensity at 580 nm significantly decreases as temperature is increased, representing positive thermal quenching. The thermal quenching temperature ($T_{0.5}$), defined as the temperature at which the emission intensity is 50% of its original value, is approximately determined to be 255 °C.[55] The temperature dependence of the PL intensity can be described by the Arrhenius equation, from which the activation energy can be accordingly calculated:[17,55]

$$I(T) = \frac{I_0}{1 + c\exp\left(\frac{-\Delta E}{kT}\right)} \quad (8)$$

where $I(T)$ is the emission intensity at a given temperature T, I_0 is the initial intensity at room temperature, c is a constant for a certain host, k is Boltzmann's constant with the value of 8.269×10^{-5} eV, and ΔE represents the activation energy for thermal quenching. Fig. 13b shows the plot and linear fitting curve of $\ln[(I_0/I_T) - 1]$ *versus* $1000/T$ for Dy^{3+} in the $LiInTi_2O_6$:0.01Tm^{3+},0.015Dy^{3+} phosphor. Thus, the value of the activation energy ΔE is determined to be 0.23 eV, calculated from the slope of the fitting line. This value of activation energy is relatively high, or comparable to other previously reported thermally stable phosphors.[49,56,57] Furthermore, when the temperature was raised up to 150 °C, which is the long-time application temperature for LEDs, the PL intensities for Tm^{3+} and Dy^{3+} respectively change to 108% and 78% of the initial intensity at room temperature. These results indicate that the $LiInTi_2O_6$:Tm^{3+},Dy^{3+} phosphor has an outstanding thermal stability against temperature quenching.

A qualitative explanation for the thermal quenching behaviour of phosphors can be obtained from the one-dimensional configuration coordinate model.[42] Fig. 14 shows the configuration coordinate diagram of Tm^{3+} and Dy^{3+} in the $LiInTi_2O_6$ host. Ideally, under excitation, the 4f electrons of Tm^{3+} and Dy^{3+} are promoted from the ground states (point A in curve ground state) into the excited states (point B1 and B2 in curve E_{Tm} and E_{Dy}),

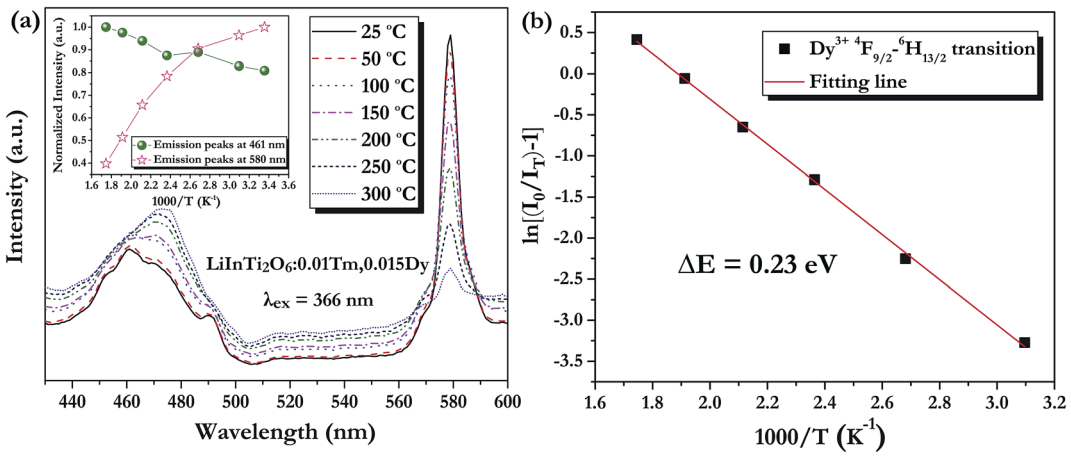

Fig. 13 (a) PL spectra of $LiInTi_2O_6$:0.01Tm^{3+},0.015Dy^{3+} phosphor upon excitation at 366 nm at different temperatures in the range of 25–300 °C. The inset shows the variation of temperature-dependent normalized intensities of Tm^{3+} and Dy^{3+} with increased temperature. (b) The activation energy for thermal quenching of Dy^{3+} in $LiInTi_2O_6$:0.01Tm^{3+},0.015Dy^{3+} phosphor.

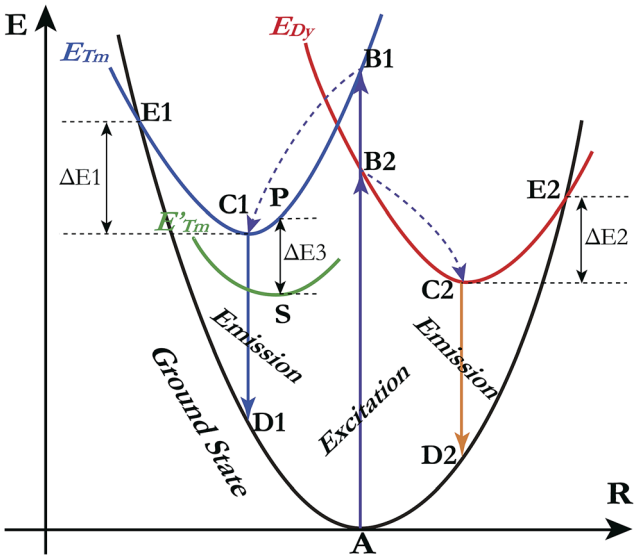

Fig. 14 Schematic illustration of thermal quenching behaviour for $LiInTi_2O_6$:0.01Tm^{3+},0.015Dy^{3+} phosphor with a configuration coordinate diagram.

then quickly relax to the lowest energy level of the excited states (point C1 and C2) by multi-phonon emission and return to the ground state, accompanied by radiative transition emissions corresponding to lines C1D1 and C2D2. However, nonradiative processes, *e.g.* thermal quenching, will always compete with radiative processes in luminescence materials. As seen in Fig. 14, as the temperature increases, the excited electrons are thermally activated *via* electron–phonon interactions to the intersection (point E1 and E2) between the ground state and excited state. By means of the crossing (point E1 and E2) it is possible to return to the ground state (point A) in a nonradiative manner by means of multiphonon relaxation. The excitation energy is then partially given up as heat to the lattice, giving rise to thermal quenching. The energy difference, ΔE, needed to be overcome in this process, between the relaxed excited state and the cross, is exactly the activation energy of thermal quenching for activators;[46,58] the larger its value, the greater the thermal stability of the phosphors. For Tm^{3+}, the NTQ means that with increasing temperature, thermal excitation of electrons from the sublevel excited state (curve E'_{Tm}) to the initial excited state (curve E_{Tm}) cannot be ignored. The electrons excited from sublevels (line SP) will compensate for the loss of electrons by nonradiative transition *via* point E1. Certainly, the energy ($\Delta E3$) required to overcome thermal excitation should be smaller than that for electron–phonon interaction to the intersection ($\Delta E1$).

3.4. Comparison of crystal structures of representative titanates

A comprehensive understanding of the chemical bonding and coordination geometry of titanates is necessary to design and select the appropriate phosphor hosts. The initial aim of this work was to design material in the Li_2O–In_2O_3–TiO_2 system with crystal structure similar to the perovskite $(ALn)_{0.5}TiO_3$. In effect, in spite of the obtained compound $LiInTi_2O_6$ having a similar formula to $(ALn)_{0.5}TiO_3$, it presents absolutely different ionic coordination environments and structural symmetry, compared to that of $(ALn)_{0.5}TiO_3$. In most cases, crystal field environments for transition metal ions in crystal structures generally possess octahedral or tetrahedral symmetry. Nevertheless, the special case of the titanium ion with 12-fold coordinated hexagonal prismatic symmetry in $LiInTi_2O_6$ is noted in this work. Herein, we sketchily elucidate the structure distinction of several titanates, providing helpful information for photo/electrical material design.

The well-known titanate compounds that are extensively applied in functional materials are the perovskite family. The ideal perovskite-type titanates generally crystallize in a cubic system with space group of $Pm\bar{3}m$ (S.G. No. 221, O_h^1), such as $SrTiO_3$, having Ti^{4+} coordinated with 6 oxygens to form corner-sharing TiO_6 regular octahedra and Sr^{2+} located at the 12-fold coordinated interstices of TiO_6 groups.[59] By full or partial substitution of suitable cations in Sr^{2+} sites, different types of modified perovskites can be obtained. They demonstrate deviations from ideal perovskite either by changes in constituents, or distortions and tilting of TiO_6 octahedra, or a combination of both,[60,61] giving rise to differences in coordination circumstances and bond connectivity. The detailed information for crystal structures of $ATiO_3$ titanates are summarized in Table 4. Ideal perovskite-type $SrTiO_3$ has a regular TiO_6 group with equal Ti–O bond lengths, and Ti–O–Ti bond angle equal to 180°. With either Ca^{2+} or Ba^{3+}, having a slightly smaller or larger ionic radius, being substituted for the Sr^{2+} ions in the cubic lattice, the electronic interaction between cations and ligands will change, so as to influence the crystal structure.[62,63] As a result, regular TiO_6 groups are distorted with one Ti–O bond stretched and the opposite one compressed, as well as Ti–O–Ti bond angles deviating from 180° linear connectivity. The family of $(Li_{0.5}Ln_{0.5})TiO_3$ perovskites, with Ln ionic radius smaller than 0.95 Å, are isomorphic to $CaTiO_3$, with Li^+ and Ln^{3+} co-occupying the same Ca^{2+} site.[64] With the ionic radius of Ln^{3+} decreasing, the degree of distortion and tilting of TiO_6 octahedra increases. Generally, the Ti–O–Ti bond angles decrease, accompanied by the decrease in covalence of chemical bonds between Ti and O, resulting in the decrease in band widths and the increase in band gap due to the increase in electron delocalisation;[19,65,66] it is therefore necessary to obtain further deep theoretical and experimental insights into the structure–property relationship for this series of compounds. When In^{3+} with a smaller ionic radius replaces Ln^{3+}, TiO_6 octahedra do not exist and polyhedra connection changes from corner-sharing to face-sharing, presenting different bonding styles. Considering having a smaller ionic radius and the same ionic valence as Ln^{3+} and In^{3+}, the imaginary compound $(Li_{0.5}Sc_{0.5})TiO_3$ with the same crystal structure of either $(Li_{0.5}Ln_{0.5})TiO_3$ or $(Li_{0.5}In_{0.5})TiO_3$ is expected to be synthesized. Furthermore, the compounds $(Na_{0.5}In_{0.5})TiO_3$ and $(K_{0.5}In_{0.5})TiO_3$, which are isomorphous to $(Li_{0.5}In_{0.5})TiO_3$, are also expected to exist in view of Na, K and Li being congener elements; however, in future work, their existence needs to be confirmed *via* experiment. It can therefore be concluded that chemical unit

Table 4 The comparison of detailed information of crystal structures for $ATiO_3$ titanates

Compound	Structure	Space group	Coordination geometry	Site symmetry	Ti–O–Ti angle	Ti–O bond length (Å)	Ref.
$SrTiO_3$	Cubic	$Pm\bar{3}m$ (221)	Sr: 12-fold cuboctahedron Ti: 6-fold regular octahedron	Sr: $m\bar{3}m$ Ti: $m\bar{3}m$	180°	Ti–O: 1.9550 × 6	59
$BaTiO_3$	Tetragonal	$P4mmm$ (99)	Ba: 12-fold cuboctahedron Ti: 6-fold octahedron	Ba: $4mmm$ Ti: $4mmm$	Ti–O1–Ti: 180° Ti–O2–Ti: 171°	Ti–O1: 1.8802 Ti–O2: 2.0043 × 4 Ti–O1: 2.1338	63
$CaTiO_3$	Orthorhombic	$Pnma$ (62)	Ca: 8-fold side-bicapped trigonal prism Ti: 6-fold octahedron	Ca: m Ti: −1	Ti–O1–Ti: 147.3° Ti–O2–Ti: 146.8°	Ti–O1: 1.9845 × 2 Ti–O2: 1.9927 × 2 Ti–O1: 1.9969 × 2	62
$Li_{0.5}Gd_{0.5}TiO_3$	Orthorhombic	$Pnma$ (62)	Li/Gd: 8-fold side-bicapped trigonal prism Ti: 6-fold octahedron	Li/Gd: m Ti: −1	Ti–O1–Ti: 148.0° Ti–O2–Ti: 146.4°	Ti–O1: 2.0238 × 2 Ti–O2: 1.9688 × 2 Ti–O1: 2.0695 × 2	64
$Li_{0.5}Y_{0.5}TiO_3$	Orthorhombic	$Pnma$ (62)	Li/Y: 8-fold side-bicapped trigonal prism Ti: 6-fold octahedron	Li/Y: m Ti: −1	Ti–O1–Ti: 147.9° Ti–O2–Ti: 146.7°	Ti–O1: 2.0047 × 2 Ti–O2: 1.9625 × 2 Ti–O1: 2.0492 × 2	64
$Li_{0.5}Lu_{0.5}TiO_3$	Orthorhombic	$Pnma$ (62)	Li/Lu: 8-fold side-bicapped trigonal prism Ti: 6-fold octahedron	Li/Lu: m Ti: −1	Ti–O1–Ti: 148.1° Ti–O2–Ti: 146.3°	Ti–O1: 2.0119 × 2 Ti–O2: 1.9491 × 2 Ti–O1: 2.0595 × 2	64
$LiInTi_2O_6$	Trigonal	$R\bar{3}m$ (166)	Li/In/Ti: 12-fold hexagonal prism	Li/In/Ti: $3m$	Ti3–O1–Ti3: 102.7° Ti4–O2–Ti4: 103.1°	Ti3–O1: 1.8444 × 6 Ti3–O1: 1.9736 × 6 Ti4–O2: 1.7946 × 6 Ti4–O2: 2.1201 × 6	This work

substitution has provided an effective means and many opportunities for designing and exploring novel functional materials.

4. Conclusions

Sub-solidus phase relationships of the Li_2O–In_2O_3–TiO_2 ternary system were determined to be composed of seven three-phase regions separated by two-phase join-lines. A new ternary compound, $LiInTi_2O_6$, was discovered and synthesized. Its thermal stability was investigated and found to endothermically decompose in the range of 1100–1200 °C *via* a four-phase transformation reaction. The crystal structure of $LiInTi_2O_6$ was solved by the charge-flipping method and refined by the Rietveld method on the basis of powder XRD data. $LiInTi_2O_6$ crystallizes in a trigonal unit cell with lattice parameters of $a = b = 5.1050(1)$ Å, $c = 28.5622(4)$ Å, and $Z = 6$ in space group $R\bar{3}m$ (No. 166), consisting of a three-dimensional structural framework constructed by distorted 12-fold coordination hexagonal prisms, which stack layer by layer along the *c* axis *via* edge-sharing and face-sharing. Taking $LiInTi_2O_6$ as the host, a series of Dy^{3+}/Tm^{3+} singly-doped and co-doped phosphors were successfully synthesized. The energy transfer process from Tm^{3+} to Dy^{3+} in $LiInTi_2O_6$:0.01Tm^{3+},Dy^{3+} phosphors was systematically demonstrated by studying their photoluminescence emission spectra and decay curves. The energy transfer efficiency η_{ET} was increased with the increment of Dy^{3+} contents. The interaction mechanism for energy transfer was determined to conform to a non-radiative electric dipole–dipole (d–d) interaction with critical distance of 20.17 Å between Tm^{3+} and Dy^{3+}. By properly adjusting the concentration of activators, the color tone of $LiInTi_2O_6$:Tm^{3+},Dy^{3+} phosphors can be tuned from blue to white across the white lighting region. Moreover, the negative thermal quenching (NTQ) phenomenon is observed in this white lighting phosphor and results in excellent thermal stability against temperature quenching. The thermal quenching behaviour is qualitatively explained by the one-dimensional configuration coordinate model. The present results indicate that $LiInTi_2O_6$:Tm^{3+},Dy^{3+} phosphors may potentially be applied as single-component colour-tuneable candidates in UV-pumped white LEDs.

Conflict of interest

The authors declare no competing financial interest.

Acknowledgements

Financial supports by grants from the National Key Research and Development Plan (No. 2016YFB0701301), the National Natural Science Foundation of China (No. 51472273), the Major State Basic Research Development Program of China (No. 2014CB6644002), the outstanding graduate project of Advanced Non-ferrous Metal Structural Materials and Manufacturing Collaborative Innovation Center (No. 510070027), and the Project of Innovation-driven Plan in Central South University (No. 2015CX004) are gratefully acknowledged.

References

1 N. Bardsley, S. Bland, L. Pattison, M. Pattison, K. Stober, F. Welsh and M. Yamada, *Solid-State Lighting Research and Development: Multi-Year Program Plan, Solid-State Lighting Program, Building Technologies Office, Office of Energy Efficiency and Renewable Energy*, U.S. Department of Energy, Washington D.C, 2014.
2 N. Bardsley, S. Bland, M. Hansen, L. Pattison, M. Pattison, K. Stober and M. Yamada, *Solid-State Lighting R&D Plan, Solid-State Lighting Program, Building Technologies Office, Office of Energy Efficiency and Renewable Energy*, U.S. Department of Energy, Washington D.C, 2015.
3 J. Y. Tsao, H. D. Saunders, J. R. Creighton, M. E. Coltrin and J. A. Simmons, *J. Phys. D: Appl. Phys.*, 2010, **43**, 354001.
4 M. H. Crawford, *IEEE J. Sel. Top. Quantum Electron.*, 2009, **15**, 1028–1040.
5 S. Pimputkar, J. S. Speck, S. P. DenBaars and S. Nakamura, *Nat. Photonics*, 2009, **3**, 180–182.
6 M. Shang, C. Li and J. Lin, *Chem. Soc. Rev.*, 2014, **43**, 1372–1386.
7 J. H. Oh, S. J. Yang and Y. R. Do, *Light: Sci. Appl.*, 2014, **3**, e141.
8 C. Branas, F. J. Azcondo and J. M. Alonso, *IEEE Industrial Electronics Magazine*, 2013, **7**, 6–14.
9 N. C. George, K. A. Denault and R. Seshadri, *Annu. Rev. Mater. Res.*, 2013, **43**, 481–501.
10 Z. Xia, C. Ma, M. S. Molokeev, Q. Liu, K. Rickert and K. R. Poeppelmeier, *J. Am. Chem. Soc.*, 2015, **137**, 12494–12497.
11 G. Li, C. C. Lin, W. T. Chen, M. S. Molokeev, V. V. Atuchin, C. Y. Chiang, W. Zhou, C. W. Wang, W. H. Li, H. S. Sheu, T. S. Chan, C. Ma and R. S. Liu, *Chem. Mater.*, 2014, **26**, 2991–3001.
12 X. J. Wang, L. Wang, T. Takeda, S. Funahashi, T. Suehiro, N. Hirosaki and R. J. Xie, *Chem. Mater.*, 2015, **27**, 7689–7697.
13 M. Chen, Z. Xia, M. S. Molokeev and Q. Liu, *Inorg. Chem.*, 2015, **54**, 11369–11376.
14 X. Zhang and M. Gong, *Dalton Trans.*, 2014, **43**, 2465–2472.
15 N. Liu, J. Y. Si, G. M. Cai and Y. Tao, *RSC Adv.*, 2016, **6**, 50797–50807.
16 Z. Leng, L. Li, X. Che and G. Li, *Mater. Des.*, 2017, **118**, 245–255.
17 Q. Q. Zhu, L. Wang, N. Hirosaki, L. Y. Hao, X. Xu and R. J. Xie, *Chem. Mater.*, 2016, **28**, 4829–4839.
18 S. K. Gupta, P. S. Ghosh, A. K. Yadav, N. Pathak, A. Arya, S. N. Jha, D. Bhattacharyya and R. M. Kadam, *Inorg. Chem.*, 2016, **55**, 1728–1740.
19 Y. Inaguma, T. Tsuchiya and T. Katsumata, *J. Solid State Chem.*, 2007, **180**, 1678–1685.
20 G. Blasse and A. Bril, *J. Chem. Phys.*, 1968, **48**, 3652–3656.
21 G. Cai, X. L. Chen, W. Y. Wang, Y. F. Lou, J. Liu, J. T. Zhao and H. H. Chen, *J. Solid State Chem.*, 2008, **181**, 646–651.
22 L. Su, X. Fan, G. Cai and Z. Jin, *Ceram. Int.*, 2016, **42**, 15994–16006.
23 L. Palatinus and G. Chapuis, *J. Appl. Crystallogr.*, 2007, **40**, 786–790.
24 V. Petříček, M. Dušek and L. Palatinus, *Z. Kristallogr.*, 2014, **229**, 345–352.
25 H. Rietveld, *Acta Crystallogr.*, 1967, **22**, 151–152.
26 J. Rodríguez-Carvajal, *Phys. B*, 1993, **192**, 55–69.
27 T. Gaewdang, J. P. Chaminade, P. Gravereau, A. Garcia, C. Fouassier, P. Hagenmuller and R. Mahiou, *Mater. Res. Bull.*, 1993, **28**, 1051–1060.
28 R. Hoppe and B. Schepers, *Z. Anorg. Allg. Chem.*, 1958, **295**, 233–240.
29 F. Stewner and R. Hoppe, *Z. Anorg. Allg. Chem.*, 1970, **374**, 239–258.
30 G. Izquierdo and A. R. West, *Mater. Res. Bull.*, 1980, **15**, 1655–1660.
31 H. Kleykamp, *Fusion Eng. Des.*, 2002, **61–62**, 361–366.
32 J. C. Mikkelsen, *J. Am. Ceram. Soc.*, 1980, **63**, 331–335.
33 L. Akselrud and Y. Grin, *J. Appl. Crystallogr.*, 2014, **47**, 803–805.
34 G. Oszlanyi and A. Suto, *Acta Crystallogr., Sect. A: Found. Crystallogr.*, 2004, **60**, 134–141.
35 C. K. Jørgensen, *Mol. Phys.*, 1962, **5**, 271–277.
36 J. L. Sommerdijk and A. Bril, *J. Electrochem. Soc.*, 1975, **122**, 952–954.
37 X. Liu, Y. Lü, C. Chen, S. Luo, Y. Zeng, X. Zhang, M. Shang, C. Li and J. Lin, *J. Phys. Chem. C*, 2014, **118**, 27516–27524.
38 Y. Lü, X. Tang, L. Yan, K. Li, X. Liu, M. Shang, C. Li and J. Lin, *J. Phys. Chem. C*, 2013, **117**, 21972–21980.
39 X. Min, M. Fang, Z. Huang, Y. Liu, C. Tang and X. Wu, *J. Am. Ceram. Soc.*, 2015, **98**, 788–794.
40 Y. Shi, Y. Wang and Z. Yang, *J. Alloys Compd.*, 2011, **509**, 3128–3131.
41 Q. Su, Z. Pei, L. Chi, H. Zhang, Z. Zhang and F. Zou, *J. Alloys Compd.*, 1993, **192**, 25–27.
42 S. Shionoya, W. M. Yen and H. Yamamoto, *Phosphor handbook*, CRC press, 2006.
43 Y. Liu, Y. Yang, G. Qian, Z. Wang and M. Wang, *Mater. Sci. Eng., B*, 2007, **137**, 74–79.
44 T. Grzyb, *RSC Adv.*, 2014, **4**, 2590–2595.
45 G. Blasse, *Phys. Lett. A*, 1968, **28**, 444–445.
46 J. Zhou and Z. Xia, *J. Mater. Chem. C*, 2015, **3**, 7552–7560.
47 D. L. Dexter and J. H. Schulman, *J. Chem. Phys.*, 1954, **22**, 1063–1070.
48 J. S. Kim, Y. H. Park, S. M. Kim, J. C. Choi and H. L. Park, *Solid State Commun.*, 2005, **133**, 445–448.
49 Z. Xia, X. Wang, Y. Wang, L. Liao and X. Jing, *Inorg. Chem.*, 2011, **50**, 10134–10142.
50 M. Watanabe, M. Sakai, H. Shibata, C. Satou, S. Satou, T. Shibayama, H. Tampo, A. Yamada, K. Matsubara, K. Sakurai, S. Ishizuka, S. Niki, K. Maeda and I. Niikura, *Phys. B*, 2006, **376–377**, 711–714.
51 M. Hauser, A. Hepting, R. Hauschild, H. Zhou, J. Fallert, H. Kalt and C. Klingshirn, *Appl. Phys. Lett.*, 2008, **92**, 211105.
52 X. H. Huang, C. Zhang, C. B. Tay, T. Venkatesan and S. J. Chua, *Appl. Phys. Lett.*, 2013, **102**, 111106.
53 F. Kang, M. Peng, Q. Zhang and J. Qiu, *Chem.–Eur. J.*, 2014, **20**, 11522–11530.
54 S. Hajime, *Jpn. J. Appl. Phys.*, 1998, **37**, 550.
55 S. Zhang, Y. Nakai, T. Tsuboi, Y. Huang and H. J. Seo, *Chem. Mater.*, 2011, **23**, 1216–1224.

56 X. Chen, Z. Xia and Q. Liu, *Dalton Trans.*, 2014, **43**, 13370–13376.
57 N. Zhang, C. Guo, J. Zheng, X. Su and J. Zhao, *J. Mater. Chem. C*, 2014, **2**, 3988–3994.
58 G. H. Muñoz, C. L. de la Cruz, A. F. Muñoz and J. O. Rubio, *J. Mater. Sci. Lett.*, 1988, **7**, 1310–1312.
59 M. A. Peña and J. L. G. Fierro, *Chem. Rev.*, 2001, **101**, 1981–2018.
60 A. Glazer, *Acta Crystallogr., Sect. B: Struct. Crystallogr. Cryst. Chem.*, 1972, **28**, 3384–3392.
61 A. Glazer, *Acta Crystallogr., Sect. A: Cryst. Phys., Diffr., Theor. Gen. Crystallogr.*, 1975, **31**, 756–762.
62 M. L. Moreira, E. C. Paris, G. S. do Nascimento, V. M. Longo, J. R. Sambrano, V. R. Mastelaro, M. I. B. Bernardi, J. Andrés, J. A. Varela and E. Longo, *Acta Mater.*, 2009, **57**, 5174–5185.
63 K. C. Huang, T. C. Huang and W. F. Hsieh, *Inorg. Chem.*, 2009, **48**, 9180–9184.
64 A. G. Belous, G. N. Novitskaya and S. V. Polyanetskaya, *Inorg. Mater.*, 1987, **23**, 1177–1179.
65 M. Wiegel, M. Hamoumi and G. Blasse, *Mater. Chem. Phys.*, 1994, **36**, 289–293.
66 G. Blasse and L. G. J. De Haart, *Mater. Chem. Phys.*, 1986, **14**, 481–484.